Available online at www.sciencedirect.com
ScienceDirect
Trans. Nonferrous Met. Soc. China 28(2018) 1670−1678
Transactions of Nonferrous Metals Society of China
www.tnmsc.cn

Numerical modeling of effect of slot on bubble motion in aluminum electrolytic process

Qiang WANG[1,2], Mei-jia SUN[3], Bao-kuan LI[3], Guang-qiang LI[1,2], Jian-ping PENG[3]

1. State Key Laboratory of Refractories and Metallurgy, Wuhan University of Science and Technology, Wuhan 430081, China;
2. Key Laboratory for Ferrous Metallurgy and Resources Utilization of Ministry of Education, Wuhan University of Science and Technology, Wuhan 430081, China;
3. School of Metallurgy, Northeastern University, Shenyang 110819, China

Received 18 May 2017; accepted 8 September 2017

Abstract: A transient three-dimensional (3D) model was established to understand the bubble motion in an industrial electrolytic process. An anode with a new design was tested. It incorporates two slots that allow an efficient removal of gas bubbles. The electromagnetic fields were described by solving Maxwell's equations. The bubble movement was studied with two-way coupling Euler−Lagrange approach. The interplay of current density and bubble nucleation rate was included. The collision and coalescence of bubbles were considered. Random walk module was invoked for involving the chaotic effect of the turbulence. The numerical results were validated by experimental measurements. The results indicate that the current distribution and the bubble nucleation periodically change. Due to the slot, the bubble elimination heavily increases. The contribution of the slot to the bubble removal exceeds 50% in the case of three currents, and the promotion of the slot decays with increasing the current.

Key words: aluminum electrolytic process; anodic bubble; slot; Euler−Lagrange approach; numerical simulation

1 Introduction

Gas generation occurs in various electrochemical reactions. Small bubbles are nucleated on the anode surface, then glide along the surface under the action of various forces, and meanwhile grow up through coalescence. These bubbles will detach from the surface once its size over a certain value, which forms a bubbly two-phase flow in the electrochemical reactor. The behaviors of bubbles such as nucleation, growth, coalescence and detachment significantly affect the current distribution and increase the energy consumption due to the ohmic drop [1]. Changes in the structure of the anode therefore have occurred so as to promote the gas bubble release. Figure 1 shows a novel anode which has been widely used in the industrial aluminum electrolysis process. A direct current (DC) passes through conductive electrolyte and molten aluminum between anode and cathode, and gas bubbles would be formed at the anode bottom and side wall because of the electrochemical reaction. In order to reduce the gas holdup, two vertical slots are incorporated in the anode.

Many researchers have experimentally studied the bubble migration in the electrolytic cell by using air−water models [2−4]. One or two anodes were suspended within a transparent tank. Gas evolution was simulated by injecting air. A high speed camera was employed to observe the two-phase flow, and a particle image velocimetry (PIV) technique was used to measure the velocity field. However, the electric current, which is a critical part of the process, was not taken into account. ALAM et al [5] implemented a low temperature electrolytic experiment. $CuSO_4$ solution was adopted as bath solution. A lead alloy and a stainless steel were used as the anode and cathode, respectively. A DC power supply was utilized to supply the current, and O_2 bubbles were generated underneath the anode. They found that the bubble movement and bubble layer thickness were sensitive to the anodic current density. With increasing computational resources, some researchers numerically investigated the bubbly two-phase flow in the cell [6−8].

Foundation item: Project (51434005) supported by the National Natural Science Foundation of China
Corresponding author: Bao-kuan LI; Tel: +86-24-83672216; Fax: +86-24-22906316; E-mail: libk@smm.neu.edu.cn
DOI: 10.1016/S1003-6326(18)64810-1

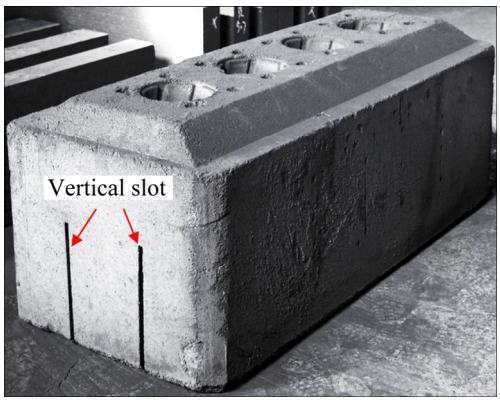

Fig. 1 Photo of novel anode

WANG et al [9] developed a mathematical model to investigate the effect of gas bubble on cell voltage oscillations. The results showed that higher bubble release frequency has a greater effect on the cell voltage oscillation, especially when the frequency is larger than 0.4 Hz. The volume of fluid (VOF) approach was widely invoked to understand the bubble behavior, because it is an efficient and robust algorithm for the multiphase flow. WANG et al [1] calculated the bubble morphology in the cell with slotted anode using the VOF method. Their results indicated that the slot provided an alternative for gas bubbles to escape. Nevertheless, the force acting on the bubbles and the coalescence of the bubbles were not included. Euler-Euler model was also employed to consider the motion of bubbles [10,11]. The interaction and the coalescence between the bubbles were taken into account. However, the coupling between the bubble nucleation and current density on the anode surface was not factored. Because it is difficult to couple the magnetohydrodynamic (MHD) model with the Euler-Euler model. Euler-Lagrange model, which could better cooperate with the MHD model, was then employed. HREIZ et al [12] used a two-way coupling discrete phase model to calculate the bubble movement in a vertical plane electrode reactor. The effect of the anodic current density on the bubble nucleation was included. The simulated results were in good agreement with the PIV measurement data.

As discussed above, there have been few attempts to numerically investigate the electromagnetic fields and bubbly two-phase flow in the aluminum electrolytic process. Because of this, we were motivated to establish a 3D comprehensive model to understand the impact of the slot on the bubble movement in the electrolytic cell. The current distribution and the Lorentz force field were described by solving Maxwell's equations. With the two-way coupling Euler−Lagrange approach, the bubble migration behavior was demonstrated. Moreover, the relationship between the current density and the bubble nucleation rate was included. Besides, an experiment was carried out to validate the model.

2 Experimental

An experiment was carried out using two glass containers at room temperature as shown in Fig. 2. $CuSO_4$ solution was serviced as the electrolyte, and the concentration was around 0.4 mol/L. A cooper plate, which was used as the cathode, was placed at the tank bottom [5,13]. The anodes without and with the slots, which were produced by graphite, were then immersed into the electrolyte in the two tanks, respectively. The distance between the anode and the cathode was fixed at 40 mm. A DC power was implemented to supply a constant 375 A current for the two electrolytic processes, i.e., the average current density on anode was 0.3 A/cm^2 [14]. A high speed camera was employed to observe the bubble morphology, and a multimeter was utilized to measure the voltage drop between the anode and the cathode [15].

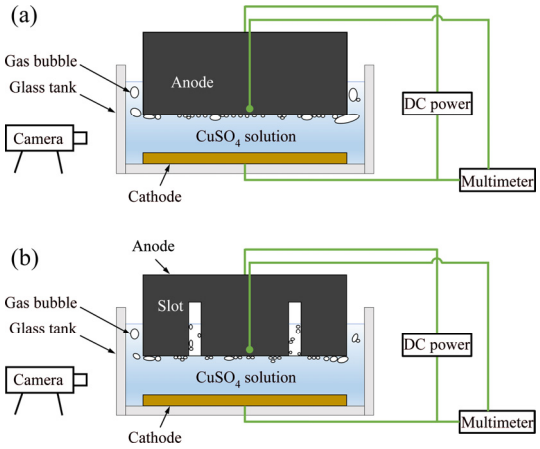

Fig. 2 Schematics of experimental setup: (a) Cell with traditional anode; (b) Cell with novel anode

3 Mathematical modeling

3.1 Electromagnetism

The current in the cell was governed by the equations of charge conservation and Ohm's law:

$$\nabla \cdot \boldsymbol{J} = 0 \tag{1}$$

$$\boldsymbol{J}=\sigma(\boldsymbol{E}+\boldsymbol{v}\times\boldsymbol{B}) \tag{2}$$

The magnetic Reynolds number, which expresses the ratio of the magnetic convection to magnetic diffusion, remained very low in this process [16]. Thus, Eq. (2) was simplified as

$$\boldsymbol{J}=\sigma\boldsymbol{E} \tag{3}$$

The Ampère's circuital law was adopted to describe the magnetic field:

$$\nabla \times \boldsymbol{H} = \boldsymbol{J} + \frac{\partial \boldsymbol{D}}{\partial t} \tag{4}$$

The current displacement, $\partial \boldsymbol{D}/\partial t$, was much lower than the electrical conduction, which was valid if the electrical conductivity was not too small, and hence this term was neglected here [17].

The constitutive equation for the magnetic field was

$$\boldsymbol{B}=\mu \boldsymbol{H} \tag{5}$$

The electrical potential approach was employed to solve the governing equations mentioned above. It consists of simultaneously solving for the electrical potential φ, as well as the magnetic potential vector $\boldsymbol{A}$:

$$\boldsymbol{E} = -\frac{\partial \boldsymbol{A}}{\partial t} - \nabla \varphi \tag{6}$$

At the same time, the magnetic potential vector was related to the magnetic field by [17]

$$\boldsymbol{B} = \nabla \times \boldsymbol{A} \tag{7}$$

With appropriate boundary conditions, can obtain the time average Lorentz force:

$$\boldsymbol{F}_{\mathrm{e}}=\boldsymbol{J}\times\boldsymbol{B} \tag{8}$$

3.2 Electrolyte hydrodynamics

The electrolyte was assumed to be incompressible, and the flow was supposed to be Newtonian and unsteady. Besides, the heat transfer was ignored in the present work. Following these assumptions, the flow was modeled by the conservation equations of mass and momentum [12]:

$$\nabla \cdot (\rho \boldsymbol{v}) = 0 \tag{9}$$

$$\left[\frac{\partial (\rho \boldsymbol{v})}{\partial t} + \nabla \cdot (\rho \boldsymbol{v} \otimes \boldsymbol{v})\right] = -\nabla p + \mu_{\mathrm{eff}} \nabla^2 \boldsymbol{v} + \boldsymbol{F} \tag{10}$$

The force $\boldsymbol{F}$ was the coupling term with the discrete phase solver, and represented the momentum exchange due to bubbles passing through each computational element. Given the characteristic of fluid flow in the process, the RNG k–ε turbulence model was adopted to calculate the turbulent viscosity. The standard k–ε turbulence model has been developed for flows with a high Reynolds number, but the RNG k–ε turbulence model is able to capture the behavior of flows with lower Reynolds number with an appropriate treatment of the near-wall region. An enhanced wall function therefore was employed to work with the RNG k–ε turbulence model.

3.3 Bubble hydrodynamics

The motion of the bubble suspended in the electrolyte was determined by gravity, buoyancy, drag, lift and added mass forces [10]. And furthermore, a pressure gradient was created in the electrolyte due to the Lorentz force. According to the law of action and reaction, the bubble endured an electromagnetic pressure force, whose direction was opposed to that of the Lorentz force [18,19]. The added mass force was induced by the acceleration difference between the bubble and the electrolyte. Besides, we used an equivalent diameter to represent the bubble size in the calculation, because the gas bubbles were observed to be non-spherical in the experiment.

The Newton's second law was used to calculate the velocity of each bubble [20,21]:

$$\rho_{\mathrm{b}} \frac{\pi}{6} d_{\mathrm{b}}^3 \frac{\mathrm{d}\boldsymbol{v}_{\mathrm{b}}}{\mathrm{d}t} = \boldsymbol{F}_{\mathrm{g}} + \boldsymbol{F}_{\mathrm{b}} + \boldsymbol{F}_{\mathrm{d}} + \boldsymbol{F}_{\mathrm{l}} + \boldsymbol{F}_{\mathrm{a}} + \boldsymbol{F}_{\mathrm{p}} \tag{11}$$

where $\boldsymbol{F}_{\mathrm{d}}$ was the drag force, and was solved by Haider and Levenspiel's correlation. $\boldsymbol{F}_{\mathrm{p}}$ was the electromagnetic pressure force:

$$\boldsymbol{F}_{\mathrm{p}} = -\frac{3}{4}\frac{\pi d_{\mathrm{b}}^3}{6}\boldsymbol{F}_{\mathrm{e}} \tag{12}$$

The random walk model was invoked to include the chaotic effect of the turbulent motion on the bubble trajectory. A random velocity was added to the time average velocity to obtain the bubble transient velocity at each time step. Each random component of the bubble transient velocity was proportional to the local turbulent kinetic energy of the electrolyte:

$$\boldsymbol{v}_{\mathrm{b}} = \overline{\boldsymbol{v}}_{\mathrm{b}} + \boldsymbol{v}'_{\mathrm{b}}, \quad \boldsymbol{v}'_{\mathrm{b}} = \zeta\sqrt{\overline{\boldsymbol{v}'^2_{\mathrm{b}}}} = \zeta\sqrt{\frac{2k}{3}} \tag{13}$$

where ζ is a random number, normally distributed between −1 and 1 and varied at each time step.

As described above, the bubbles grow by collision and coalescence with other bubbles in the cell. Here, we considered three collision models of bubbles, which included the Brownian, Stokes and turbulent collisions as indicated in Fig. 3 [22,23]. The number of collisions per unit volume and unit time between two bubbles with sizes r_i and r_j was defined as

$$N_{ij} = \beta(r_i, r_j) n(r_i) n(r_j) \tag{14}$$

where $\beta(r_i, r_j)$ was the collision rate constant with a dimension of volume/time, also called the "collision volume" which represented the probabilities of collision and coalescence for bubbles.

Bubbles would contact, collide and coalesce each other due to the Brownian movement. The collision rate constant of the Brownian collision was given as

$$\beta_{\mathrm{l}}(r_i, r_j) = \frac{2kT}{3\mu_{\mathrm{v}}}\left(\frac{1}{r_i} + \frac{1}{r_j}\right)(r_i + r_j) \tag{15}$$

Due to a greater buoyancy, larger bubble floats faster than the smaller one. As a result, the bigger and

faster bubble swallows up the smaller and slower bubble. The collision rate constant of the Stokes collision was

$$\beta_2(r_i,r_j)=\frac{2\pi g\Delta\rho}{9\mu_v}\left|r_i^2-r_j^2\right|(r_i+r_j)^2 \quad (16)$$

Bubbles collide each other under the effect of the turbulent flow. The collision rate constant of the turbulent collision was

$$\beta_3(r_i,r_j)=1.3(r_i+r_j)^3\sqrt{\frac{\rho\varepsilon}{\mu_v}} \quad (17)$$

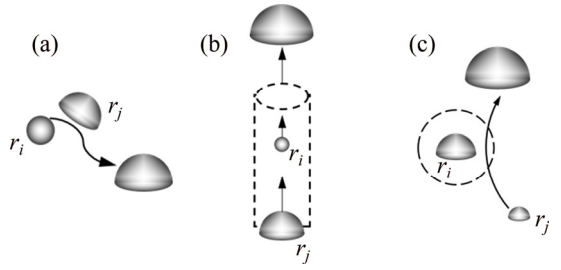

Fig. 3 Collision and coalescence of bubbles: (a) Brownian collision; (b) Stokes collision; (c) Turbulent collision

3.4 Boundary conditions

The current density and the bubble nucleation at the anode bottom and side walls were supposed to influence each other. The local current density decreases when the bubble starts to grow, and then increases once the bubble leaves the nucleation site. The bubble nucleation rate in turn depends on the local current density. In the calculation, we imposed a current density at the anode bottom and lateral walls [24,25], and moreover the volume flow rate of the bubbles on the surfaces was related to the current density [4]:

$$q=\frac{|\boldsymbol{J}|AR_{gas}T}{4pF} \quad (18)$$

where A is the area of the surfaces for the nucleation, and T is the room temperature. Meanwhile, a zero potential was applied at the bottom. Other walls were assumed to be insulated where there was no electric current going through the boundaries. The initial diameter of the nucleated bubble was actually small. We assigned a constant diameter, 1 mm, for the nucleated bubble according to our experimental observation. As for the motion of the bubble, it would be rebounded once touching the lateral wall and the bottom of the cell, and escape from the top surface of the cell. A no-slip wall was imposed at all boundaries except on the top surfaces of the slot and cell, where a zero shear stress was employed. All the physical properties remained constant. The detailed geometrical and physical properties are listed in Table 1.

Table 1 Geometrical and physical properties

Parameter	Value
Electrolyte density/(kg·m^{-3})	1195
Electrolyte viscosity/(Pa·s)	0.0011
Electrolyte electrical conductivity/(Ω^{-1}·m^{-1})	0.42
Surface tension/(N·m^{-1})	0.098
Bubble density/(kg·m^{-3})	0.38
Length of cell/m	0.505
Width of cell/m	0.26
Height of cell/m	0.09
Length of anode/m	0.41
Width of anode/m	0.165
Height of anode/m	0.1
Width of slot/m	0.005
Anode cathode distance/m	0.04
Current/A	375

4 Numerical treatment

The commercial software ANSYS FLUENT 12.1 was employed to implement the simulation. The governing equations for the electromagnetism, fluid flow and bubble movement were integrated over each control volume and solved simultaneously, using an iterative procedure. The electromagnetic fields were solved by the magnetohydrodynamic module, and the introduction of the magnetic potential vector was executed by user-defined functions. The Lorentz force was updated at each iteration as a function of the bubble distribution, and was then incorporated into the momentum equation. The widely used SIMPLE algorithm was employed for calculating the electrolyte hydrodynamics equations. All equations were discretized by the second order upwind scheme for a higher accuracy. Before advancing, the iterative procedure continues until all normalized unscaled residuals were less than 10^{-6}. The computation domain was discretized with a structured mesh, as shown in Fig. 4. Mesh independence was thoroughly tested. Three families of meshes were generated, respectively with 950000, 761000 and 520000 control volumes. After a typical simulation, we compared velocity of some points in the cell. The deviation of simulated results between the first and second mesh was about 10%, while was approximately 4% between the second and third meshes. Furthermore, the value of y+ within the first layer grid of the three meshes was equal to ~1. Considering the expensive computation, the second mesh was retained for the rest of the present work. The time step, 0.01 s, was kept small to ensure that the above convergence criteria were fulfilled. At the initial state, the cell was filled with stagnant electrolyte. We imposed

a constant current density at the bottom and lateral walls of the anode. The electrolyte then began to move, and the bubble was simultaneously generated. It was typically approximately 360 CPU hours for performing one case using 8 cores of 4.0 GHz.

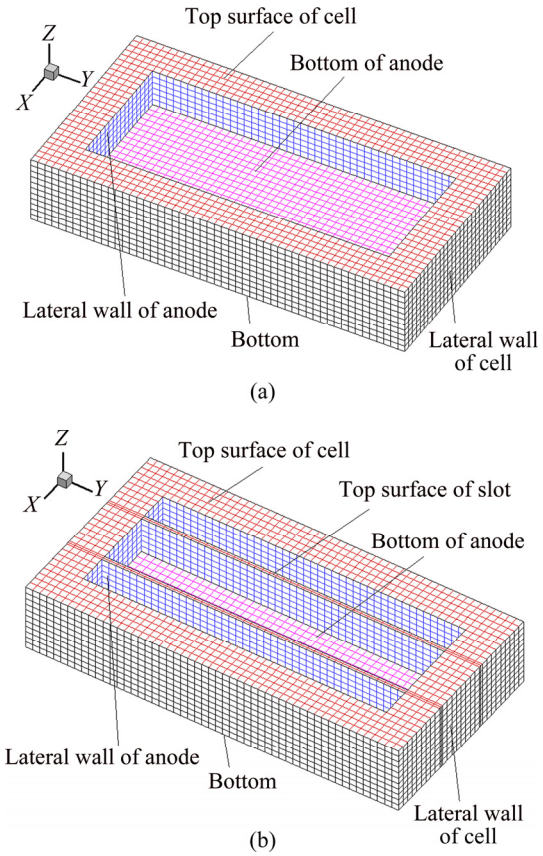

Fig. 4 Computational domains and boundaries: (a) Cell with traditional anode; (b) Cell with novel anode

5 Results and discussion

Figure 5 demonstrates the distributions of the current line and gas volume fraction at 45 s with a current of 375 A. The electric current enters the cell from the bottom and lateral walls of the anode, and meanwhile the bubbles begin to nucleate and grow due to the electrochemical reaction. As expressed by the Faraday's law, the quantity of electro-generated gas bubble is directly related to the current applied to the cell. Higher gas volume fraction is actually observed at high current density. A higher gas volume fraction induces a larger resistance, and impedes the current migration. Subsequently, the current at the bottom and lateral walls of the anode then reselects its motion path according to the electrical resistance. The current density at the place, where few bubbles are generated, rapidly increases, and in turn promotes the bubble nucleation. It is supposed that the current density distribution as well as the bubble nucleation in the cell periodically changes.

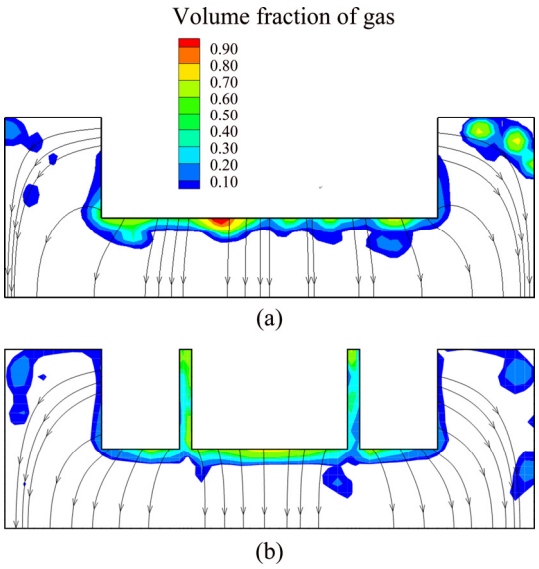

Fig. 5 Distributions of current line and gas volume fraction at 45 s with current of 375 A: (a) Cell with traditional anode; (b) Cell with novel anode

Figure 6 displays the flow pattern in the two cells at the same moment. A circulation cell and an upward flow are observed at the side channel and the slot, respectively. Tiny bubbles are formed at the anode bottom and expand through collision and coalescence, and then glide toward the outer edge of the anode bottom, and eventually detach from the anode bottom. It can be noticed that the circular flow at the side channel of the cell using the anode without slot is stronger than that of the cell using the anode with slot. Because the side channel in the cell using the anode without slot is the only release path for the bubbles, whereas in the cell using the anode with slot, the bubbles could escape from both slot and side channel.

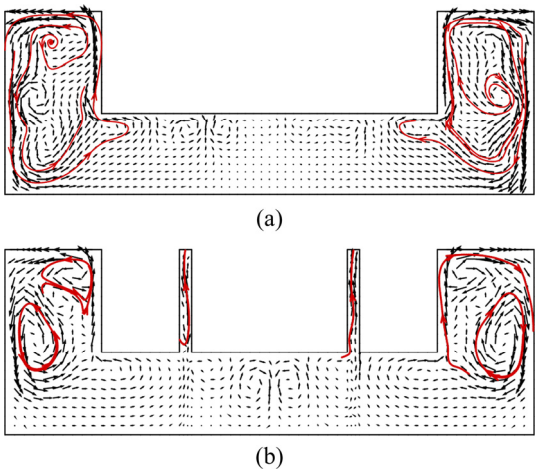

Fig. 6 Velocity field at 45 s with current of 375 A and maximum velocity of about 0.11 m/s: (a) Cell with traditional anode; (b) Cell with novel anode

Figure 7 represents the bubble distribution in the two cells at 45 s. In the cell with novel anode, bubbles escape from the slot and side channel. These bubbles could depart from the anode bottom and rise up with a small volume, since these bubbles receive less resistance during releasing. The bubbles in the cell with traditional anode are obviously bigger than that in the cell with novel anode. The maximum equivalent diameter of bubble in the cell with traditional anode reaches around 20 mm.

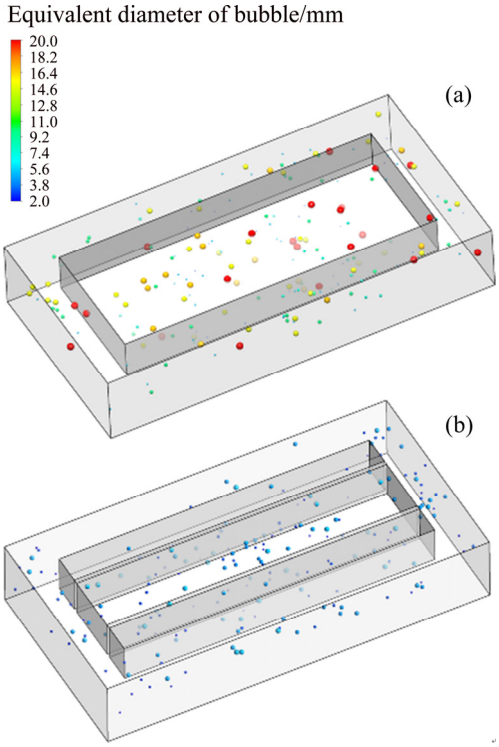

Fig. 7 Bubble distribution at 45 s with current density of 0.3 A/cm^2: (a) Cell with traditional anode; (b) Cell with novel anode

Figure 8 displays the experimental observed bubble morphology in the two cells. It is clear that the bubbles under the anode without slot is much bigger than that below the anode with slot. Because the slot provides more opportunities for the bubble to release, and as a result the bubbles could escape before growing too large. Figure 9 illustrates the comparison of the variation of the cell voltage drop between the simulation and the experiment. The simulated result closely agrees with the experimental result, which indicates the model reliability. It is clear that the ohmic drop periodically changes in the two cells. The frequency of the voltage variation of the cell using the anode without slot is around 0.63 Hz, and is lower than that of the cell using the anode with slot whose frequency is about 1.0 Hz. The voltage change is caused by the regular movements of bubbles at the bottom and lateral walls of the anode such as nucleation, coalescence, growth and detachment. Since the slot promotes the bubble movement, the bubbles release frequency in the cell with the new type anode is higher and the bubble size is smaller, which could effectively reduce the voltage fluctuation.

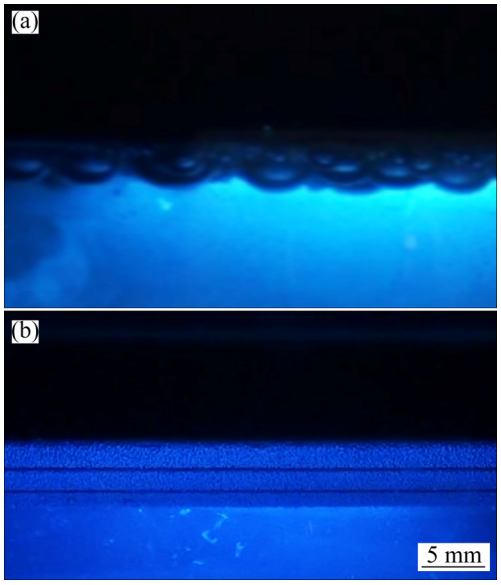

Fig. 8 Photos of bubble morphology in experiment: (a) Cell with traditional anode; (b) Cell with novel anode

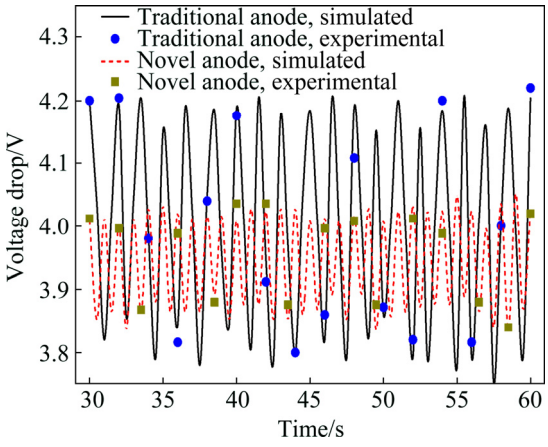

Fig. 9 Comparison of cell voltage drop between simulated results and experimental data

In the simulation, we have respectively counted up the total volumes of the new generated and the escaped bubbles within 30 s. The removal ratio of the bubbles is defined as the ratio of the total volume of the escaped bubbles to that of the new generated bubbles within the 30 s. Figure 10 indicates the removal ratio of the two cells in the case of three currents. The removal ratio significantly increases with the help of the slot, which increases by 14%, 20% and 8% respectively when the current ranges from 250 to 500 A. And the contribution of the slot to the removal ratio exceeds 50% in all cases. The increase amplitude of the removal ratio is the

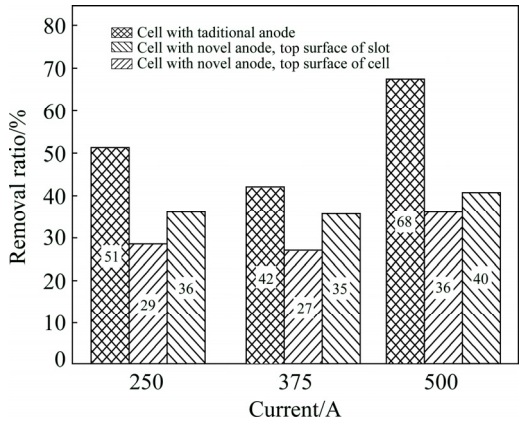

Fig. 10 Removal ratio of bubble in two cells within 30 s in case of three currents

smallest when the current is 500 A. Because the new generated bubbles underneath the anode without slot could grow big enough for the release. The influence of the slot therefore decays. Besides, the minimal removal ratios of the two cells are observed when the current is 375 A. Because both the nucleation rate and the bubble size increase with the stronger current. The increasing of the bubble size however falls behind that of the nucleation rate. The undersized new generated bubbles at the anode bottom thus cannot escape in time, causing the decrease of the removal ratio.

Figure 11 shows the distribution of the equivalent diameter of the escaped bubble within 30 s. In the two cells, the peak gradually moves to the right side with the increasing current, which indicates that higher current

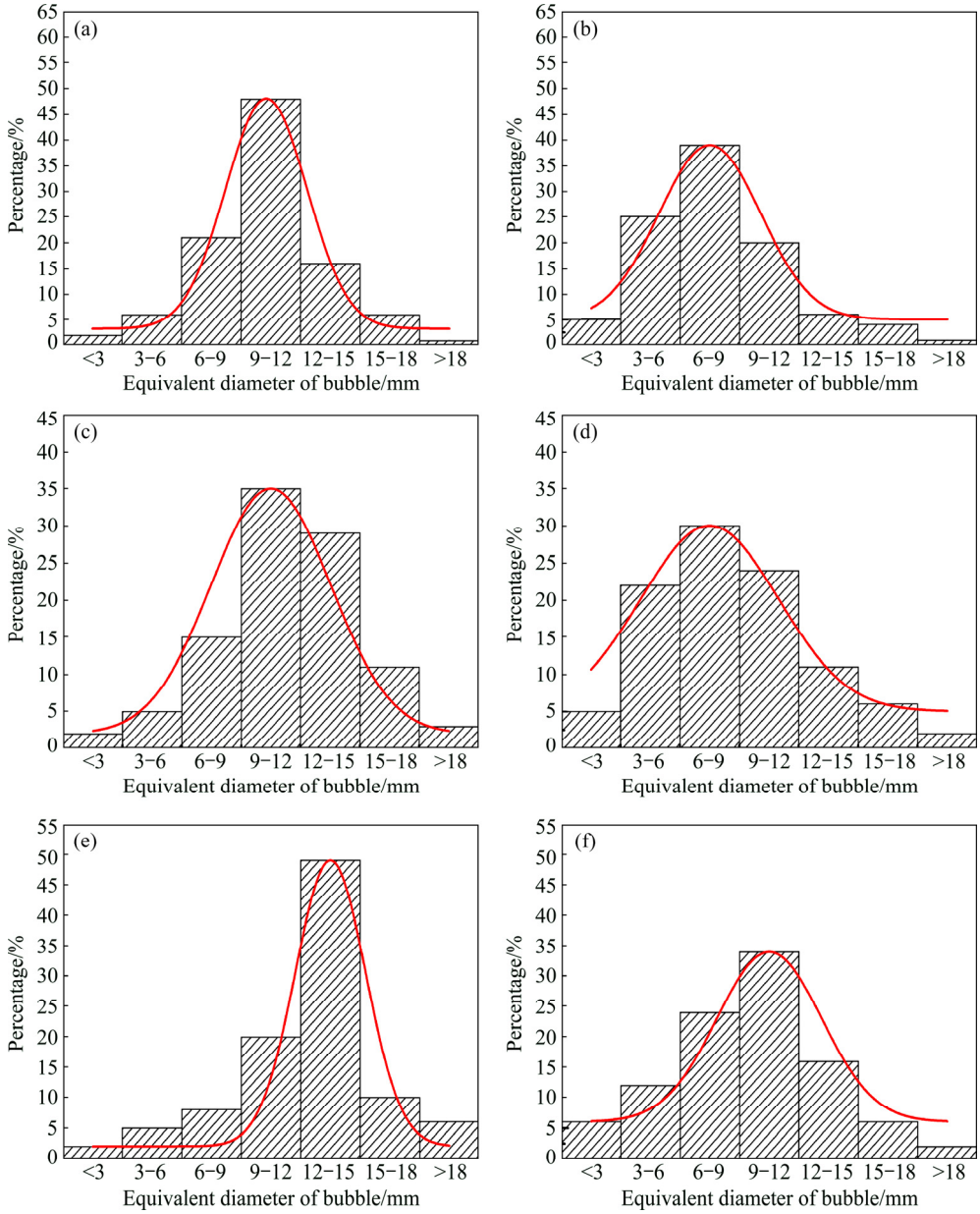

Fig. 11 Distributions of equivalent diameter of escaped bubble with traditional (a, c, e) and novel (b, d, f) anodes within 30 s: (a, b) 250 A; (c, d) 375 A; (e, f) 500 A

promotes the bubble growth. It can be seen that the proportion of the big bubble in the cell with the traditional anode is larger than that in the cell with the novel anode. Moreover, the equivalent diameter of the bubbles in the cell with the traditional anode mostly ranges from 9 to 15 mm, while the bubble size distribution has a better dispersion in the cell with the novel anode. Because the bubbles in the cell with the traditional anode can only escape when their size is over a certain value. The introduced slot however makes bubble release easier as mentioned above. Therefore, the initial volume for bubble release decreases and the range of the equivalent diameter increases.

6 Conclusions

1) Higher current density promotes the bubble nucleation and growth, and in turn the active bubble motion hinders the current flow and increases the ohmic drop. The current distribution and the bubble nucleation in the cell periodically change.

2) The removal ratio heavily increases due to the induction of the slot. The contribution of the slot to the removal ratio exceeds 50% in the case of three currents. The promotion of the slot decays with the increasing current.

3) The equivalent diameter of the bubbles in the cell with the traditional anode mostly ranges from 9 to 15 mm, while the bubble size distribution has a better dispersion in the cell with the novel anode. The proportion of the big bubble in the cell with the traditional anode is larger than that in the cell with the novel anode.

List of symbols

A Area of surfaces for bubble nucleation, m^2;
$\boldsymbol{A}$ Magnetic potential vector, V·s/m;
$\boldsymbol{B}$ Magnetic flux density, T;
$\boldsymbol{D}$ Electric flux density, C/m^2;
d_b Bubble diameter, m;
$\boldsymbol{E}$ Electric field intensity, N/C;
F Faraday's constant, A/(mol·s);
$\boldsymbol{F}$ Coupling term with discrete phase solver in Eq. (10);
$\boldsymbol{F}_a$ Added mass force, N/m^3;
$\boldsymbol{F}_b$ Buoyancy, N/m^3;
$\boldsymbol{F}_d$ Drag force, N/m^3;
$\boldsymbol{F}_e$ Lorentz force, N/m^3;
$\boldsymbol{F}_g$ Gravity, N/m^3;
$\boldsymbol{F}_l$ Lift force, N/m^3;
$\boldsymbol{F}_p$ Electromagnetic pressure force, N/m^3;
g Gravitational acceleration, m^2/s;
$\boldsymbol{H}$ Magnetic field intensity, A/m;
i, j Bubble sequence number;
$\boldsymbol{J}$ Current density, A/m^2;
k_{eff} Effective thermal conductivity, W/(m·K);
k Turbulent kinetic energy, m^2/s^2;
N_{ij} Number of collision per unit volume and per time, $m^{-3}\cdot s^{-1}$;
$n(r)$ Number density of the bubble with radius r, m^{-3};
p Pressure, Pa;
q Volume flow rate of the gas, L/min;
R_{gas} Gas constant, J/(mol·K);
r Bubble radius, m;
T Temperature, K;
t Time, s;
$\boldsymbol{v}$ Velocity, m/s;
$\boldsymbol{v}_b$ Bubble transient velocity, m/s;
$\overline{\boldsymbol{v}}_b$ Bubble mean velocity, m/s;
$\boldsymbol{v}'_b$ Bubble random velocity, m/s;
$\beta(r_i,r_j)$ Collision rate constant of r_i and r_j bubbles, m^3/s;
$\Delta\rho$ Density difference, kg/m^3;
ε Bath turbulent kinetic energy dissipation rate, m^2/s^3;
μ Magnetic permeability, F/m;
μ_{eff} Effective viscosity, Pa·s;
μ_v Dynamic viscosity, Pa·s;
ζ Random number used in Eq. (13);
ρ Density, kg/m^3;
ρ_b Bubble density, kg/m^3;
σ Electrical conductivity, $\Omega^{-1}\cdot m^{-1}$;
φ Electrical potential, V.

References

[1] WANG Yu-feng, ZHANG Li-feng, ZUO Xiang-jun. Simulation of the fluid flow-related phenomena in the electrolyte of an aluminum electrolysis cell [J]. Metallurgical and Materials Transactions B, 2011, 42(5): 1051−1064.

[2] QIAN K, CHEN J J J, MATHEOU N. Visual observation of bubbles at horizontal electrodes and resistance measurements on vertical electrodes [J]. Journal of Applied Electrochemistry, 1997, 27(4): 434−440.

[3] VÉKONY K, KISS L I. Morphology of two-phase layers with large bubbles [J]. Metallurgical and Materials Transactions B, 2010, 41(5): 1006−1017.

[4] VÉKONY K, KISS L I. Experimental study of the morphology and dynamics of gas-laden layers under the anodes in an air-water model of aluminum reduction cells [J]. Metallurgical and Materials Transactions B, 2012, 43(5): 1086−1097.

[5] ALAM M, YANG W, MOHANARANGAM K, BROOKS G, MORSI

Y S. Investigation of anodic gas film behavior in Hall–Heroult cell using low temperature electrolyte [J]. Metallurgical and Materials Transactions B, 2013, 44(5): 1155−1165.
[6] FENG Y Q, YANG W, COOKSEY M, SCHWARZ M P. Development of whole cell CFD model of bath flow and alumina mixing [J]. Journal of Computation Multiphase Flows, 2010, 2: 179−188.
[7] LI J, XU Y J, ZHANG H L, LAI Y Q. An inhomogeneous three-phase model for the flow in aluminium reduction cells [J]. International Journal of Multiphase Flow, 2011, 37(1): 46−54.
[8] WANG Q, LI B K, HE Z, FENG N X. Simulation of magnetohydrodynamic multiphase flow phenomena and interface fluctuation in aluminum electrolytic cell with innovative cathode [J]. Metallurgical and Materials Transactions B, 2014, 45(1): 272−294.
[9] WANG Yong-liang, TIE Jun, TU Gan-feng, SUN Shu-chen, ZHAO Ren-tao, ZHANG Zhi-fang. Effect of gas bubble on cell voltage oscillations based on equivalent circuit simulation in aluminum electrolysis cell [J]. Transactions of Nonferrous Metals Society of China, 2015, 25(1): 335−344.
[10] HREIZ R, ABDELOUAHED L, FÜNFSCHILLING D, LAPICQUE, F. Electrogenerated bubbles induced convection in narrow vertical cells: A review [J]. Chemical Engineering Research and Design, 2015, 100(10): 268−281.
[11] IPEK N, VYNNYCKY M, CORNELL A. A coupled electrochemical and hydrodynamical two-phase model for the electrolytic pickling of steel [J]. Journal of Electrochemical Society, 2008, 155(3): 33−43.
[12] HREIZ R, ABDELOUAHED L, FÜNFSCHILLING D, LAPICQUE F. Electrogenerated bubbles induced convection in narrow vertical cells: PIV measurements and Euler-Lagrange CFD simulation [J]. Chemical Engineering Science, 2015, 134(10): 138−152.
[13] BOISSONNEAU P, BYRNE P. An experimental investigation of bubble-induced free convection in a small electrochemical cell [J]. Journal of Applied Electrochemistry, 2000, 30(7): 767−775.
[14] QIAN K, CHEN Z D, CHEN J J J. Bubble coverage and bubble resistance using cells with horizontal electrode [J]. Journal of Applied Electrochemistry, 1998, 28(10): 1141−1145.
[15] EINARSRUD K E. The effect of detaching bubbles on aluminum-cryolite interfaces: An experimental and numerical investigation [J]. Metallurgical and Materials Transactions B, 2010, 41(3): 560−573.
[16] MUNGER D, VINCENT A. Electric boundary conditions at the anodes in aluminum reduction cells [J]. Metallurgical and Materials Transactions B, 2006, 37(6): 1025−1035.
[17] BÍRÓ O, PREIS K. On the use of the magnetic vector potential in the finite element analysis of three-dimensional eddy currents [J]. IEEE Transaction on Magnetics, 1989, 25: 3145−3159.
[18] AFSHAR M R, ABOUTALEBI M R, GUTHRIE R I L, ISAC M. Modeling of electromagnetic separation of inclusions from molten metals [J]. International Journal of Mechanical Science, 2010, 52(9): 1107−1114.
[19] WANG Q, QI F S, LI B K, TSUKIHASHI F. Behavior of non-metallic inclusions in a continuous casting tundish with channel type induction heating [J]. ISIJ International, 2014, 54(2): 2796−2805.
[20] ABDELOUAHED L, HREIZ R, PONCIN S, VALENTIN G, LAPICQUE F. Hydrodynamics of gas bubbles in the gap of lantern blade electrodes without forced flow of electrolyte: Experiments and CFD modeling [J]. Chemical Engineering Science, 2014, 111: 255−265.
[21] KIM I, ELGHOBASHI S, SIRIGNANO W A. On the equation for spherical-particle motion: Effect of Reynolds and acceleration numbers [J]. Journal of Fluid Mechanics, 1998, 367: 221−253.
[22] MIKI Y, THOMAS B G. Modeling of inclusion removal in a tundish [J]. Metallurgical and Materials Transactions B, 1999, 30(4): 639−654.
[23] ZHANG L F, TANIGUCHI S, CAI K K. Fluid flow and inclusion removal in continuous casting tundish [J]. Metallurgical and Materials Transactions B, 2000, 31(2): 253−266.
[24] ALEXIADIS A, DUDUKOVIC M P, RAMACHANDRAN P, CORNELL A, WANNGARD J, BOKKERS A. Liquid-gas flow patterns in a narrow electrochemical channel [J]. Chemical Engineering Science, 2011, 66(10): 2252−2260.
[25] PHILIPPE M, JÉRÔME B, SEBASTIEN B, GÉRARD P. Modelling and calculation of the current density distribution evolution at vertical gas-evolving electrodes [J]. Electrochimica Acta, 2005, 51(6): 1140−1156.

开槽阳极对铝电解槽中气泡运动影响的数值模拟

王 强[1,2]，孙美佳[3]，李宝宽[3]，李光强[1,2]，彭建平[3]

1. 武汉科技大学 耐火材料与冶金国家重点实验室，武汉 430081；
2. 武汉科技大学 钢铁冶金与资源利用教育部重点实验室，武汉 430081；
3. 东北大学 冶金学院，沈阳 110819

摘 要：为了研究铝电解过程中的气泡运动，建立三维非稳态数学模型。设计新型双开槽阳极，这种新型阳极可以有效去除电解过程中生成的气泡。通过求解麦克斯韦方程得到电磁场。采用双向耦合欧拉−拉格朗日方法研究气泡的运动，并且考虑电流密度与气泡形核速率之间的相互影响以及气泡的碰撞合并过程。采用随机游走模型考虑湍流的混沌效应。数值模拟结果与实验结果吻合良好。结果表明：阳极电流分布与气泡形核呈现出周期性变化，开槽阳极显著加快气泡的去除。在三组电流情况下，气泡去除率均超过 50%；随着电流的增加，开槽的作用逐渐减小。

关键词：铝电解过程；阳极气泡；开槽；欧拉−拉格朗日法；数值模拟

(Edited by Xiang-qun LI)